Temperatures near the lunar poles and their correlation with hydrogen predicted by LEND

Philipp Gläser[1], Anton Sanin[2], Jean-Pierre Williams[3], Igor Mitrofanov[2], and Jürgen Oberst[4]

[1]Technische Universität Berlin
[2]Institute for Space Research of Russian Academy of Sciences
[3]University of California Los Angles
[4]Technische Universität Berlin, Institute of Geodesy and Geoinformation Science

November 22, 2022

Abstract

The lunar polar regions offer permanently shadowed regions (PSRs) representing the only regions which are cold enough for water ice to accumulate on the surface. The Lunar Exploration Neutron Detector (LEND) aboard the Lunar Reconnaissance Orbiter (LRO) has mapped the polar regions for their hydrogen abundance which possibly resides there in the form of water ice. Neutron Suppression Regions (NSRs) are regions of excessive hydrogen concentrations and were previously identified using LEND data. At each pole we applied thermal modeling at three NSRs and one unclassified region to evaluate the correlation between hydrogen concentrations and temperatures. Our thermal model delivers temperature estimates for the surface and for 29 layers in the sub-surface down to 2 m depth. As anticipated, we find the three south polar NSRs which are coincident with PSRs in agreement with locations of hydrogen abundance and their respective (near-)surface temperatures. Water ice is suspected to be present in the upper [?]19 cm layer of regolith. The three north polar NSRs however lie in non-PSR areas and are counter-intuitive as such that most surfaces reach temperatures that are too high for water ice to exist. However, we found that these areas offer ideal conditions for ice pumping and suggest water ice to depths down to [?]35-65 cm. These depths are observable by LEND and can, at least in part, explain the existence and shape of the observed hydrogen signal. Although we can substantiate the anticipated correlation between hydrogen abundance and temperature the converse argument cannot be made.

Temperatures near the lunar poles and their correlation with hydrogen predicted by LEND

P. Gläser[1,2], A. Sanin[3], J.-P. Williams[4], I. Mitrofanov[3], J. Oberst[1,5]

[1]Technische Universität Berlin, Department of Planetary Geodesy, Str. des 17. Juni 135, 10623 Berlin, Germany
[2]Ronin Institute for Independent Scholarship, Montclair, NJ 07043, USA
[3]Institute for Space Research of Russian Academy of Sciences, Moscow 117997, Russian Federation
[4]Department of Earth, Planetary and Space Sciences, University of California Los Angeles, 595 Charles Young Drive East, Box 951567, Los Angeles, CA 90095-1567, USA
[5]German Aerospace Center, Institute of Planetary Research, Rutherfordstrasse 2, 12489 Berlin, Germany

Key Points:

- Hydrogen predicted by LEND correlates with low temperatures near the lunar poles, either at the surface or near sub-surface
- Several NSRs, or parts of it, seem to be formed through ice pumping in the sub-surface while in some NSRs ice deposits right at the surface

Corresponding author: Philipp Gläser, `philipp.glaeser@tu-berlin.de`

Abstract

The lunar polar regions offer permanently shadowed regions (PSRs) representing the only regions which are cold enough for water ice to accumulate on the surface. The Lunar Exploration Neutron Detector (LEND) aboard the Lunar Reconnaissance Orbiter (LRO) has mapped the polar regions for their hydrogen abundance which possibly resides there in the form of water ice. Neutron Suppression Regions (NSRs) are regions of excessive hydrogen concentrations and were previously identified using LEND data. At each pole we applied thermal modeling at three NSRs and one unclassified region to evaluate the correlation between hydrogen concentrations and temperatures. Our thermal model delivers temperature estimates for the surface and for 29 layers in the sub-surface down to 2 m depth. As anticipated, we find the three south polar NSRs which are coincident with PSRs in agreement with locations of hydrogen abundance and their respective (near-)surface temperatures. Water ice is suspected to be present in the upper ≈ 19 cm layer of regolith. The three north polar NSRs however lie in non-PSR areas and are counter-intuitive as such that most surfaces reach temperatures that are too high for water ice to exist. However, we found that these areas offer ideal conditions for ice pumping and suggest water ice to depths down to $\approx 35-65$ cm. These depths are observable by LEND and can, at least in part, explain the existence and shape of the observed hydrogen signal. Although we can substantiate the anticipated correlation between hydrogen abundance and temperature the converse argument cannot be made.

Plain Language Summary

The lunar poles have quite unique illumination conditions. For instance, the Sun never shines on some crater floors. As a consequence, the floors of those craters are very cold and dark. Here, water can freeze on the surface and can be preserved for long periods of time. One of the instruments mounted on the Moon-orbiting satellite Lunar Reconnaissance Orbiter (LRO) is capable of detecting areas where water ice is located. For instance, the instrument detected several areas at the lunar poles where a lot more water ice is found than at other locations. For these special locations we calculated the temperatures at the surface and near sub-surface to see whether they are indeed cold enough for water to freeze. At some of these locations, temperatures turn out to be too warm. However, we found that at these warm surfaces where no water ice can exist it can be transported into the sub-surface and survive there. This mechanism is referred to as ice pumping. In summary, we could show that temperatures at all these special locations are usually cold enough for water ice, either right at the surface or within the first meter of soil.

1 Introduction

1.1 Lunar polar environment

The lunar poles offer a unique environment where extreme illumination and thermal conditions exist in immediate vicinity to each other. Owing to the small lunar axial tilt of $1.5\,^\circ$ with respect to the ecliptic, permanently shadowed regions (PSRs) exist in many polar craters (Noda et al., 2008; Bussey et al., 2010; Mazarico et al., 2011). Consequently the coldest temperatures at the Moon are found within these craters (Paige et al., 2010) where the lowest temperatures hover at crushingly cold 20 K (Siegler et al., 2015; Williams et al., 2019). On crater rims of such PSRs, however, persistently illuminated areas can exist offering sunshine at surface level for $80-90\,\%$ of the year and even $> 90\,\%$ at two meters above ground (Gläser et al., 2014, 2018). Here temperatures of ≈ 300 K (Gläser & Gläser, 2019) are possible and hence these areas represent the opposite extreme in illumination and thermal conditions to the nearby PSRs.

1.2 Volatile sources, migration and cold trapping

Over half a century ago Watson et al. (1961) postulated the theory that water ice can be cold-trapped in lunar polar craters. Arnold (1979) proposed four potential sources for said lunar H_2O which are still valid today: solar wind reduction of iron (FeO), H_2O delivery by asteroids and/or comets, and degassing of endogenic water from the lunar interior. Independent of the source, in each of the four scenarios water molecules need to migrate to the cold polar areas in order to become trapped within PSRs. Butler et al. (1993) and Butler (1997) showed that $20-50\,\%$ of water molecules survive the migration to the poles via ballistic hops and accumulate in cold traps. In a recent study Needham and Kring (2017) estimated that volcanically-derived volatiles alone, degassed during mare basalt forming eruptions, could account for all currently observed hydrogen deposits in lunar PSRs. Crider and Vondrak (2002) showed that water deposits implanted by the solar wind proton flux within 100 Myr could also account for all hydrogen detected by the Lunar Prospector Neutron Spectrometer (LPNS) (Feldman et al., 1998). Ong et al. (2010) calculated the delivery of water via asteroidal and cometary impacts and found that either delivery mechanism could account for the observed hydrogen content by LPNS.

Those water molecules surviving migrations and are deposited in cold traps further are suspect to disruption by sputtering, impact gardening, sublimation, and bombardment by UV radiation (Ong et al., 2010). At temperatures of 110 K, for instance, it would take 1 billion years for a 1-meter-thick ice layer to evaporate (Vasavada et al., 1999). Killen et al. (1997) however showed that for temperatures < 112 K the delivery of water from meteoroids and asteroids equals or even exceeds the loss rate. Such low temperatures are commonly found within PRSs (Paige et al., 2010) suggesting that water ice can not only be trapped there but also survive geologic time-scales.

1.3 Observations

Ever since water ice was thought to exist on the Moon, a series of remote sensing techniques was applied to detect and quantify potential deposits (e.g. Nozette et al., 1996; Feldman et al., 1998; Pieters et al., 2009; Clark, 2009; Paige et al., 2010; Mitrofanov et al., 2010; Thomson et al., 2011; Zuber et al., 2012; Benna et al., 2019). Although findings of previous authors are plentiful, they cannot unambiguously be assigned to the presence of water ice but different explanations can be given, e.g. roughness, fresh surface material, hydroxyl (OH) bearing minerals etc. Nevertheless, there is direct evidence for significant amounts of lunar near-surface water ice in Cabeus crater measured directly by the Lunar Crater Observation and Sensing Satellite (LCROSS) (Colaprete et al., 2010). Cabeus' crater floor is a PSR and was selected as the LCROSS impact site due to elevated levels of hydrogen reported by both, the LPNS (Feldman et al., 1998) and the Lunar Exploration Neutron Detector (LEND) (Mitrofanov et al., 2010).

PSRs are all found near the poles in which temperatures generally are such that water ice can exist at surface level. However, Mitrofanov et al. (2012) showed that hydrogen-rich regions, the so-called neutron suppressed regions (NSRs), as identified by LEND do not necessarily coincide with PSRs. Surprisingly they can also be found in non-PSR areas where temperatures are too high for water ice to exist. These occasionally sunlit NSRs generally only occur near the lunar north pole whereas NSRs at the lunar south pole usually coincide with PSRs. Supporting evidence for the lack of hydrogen deposits in north polar PSRs is given in a study by Rubanenko et al. (2019). They evaluated depth-to-diameter ratios of simple craters at Mercury and the Moon and found that they become distinctively shallower from 75 °N/S on polewards. The shallowing is due to infill within the craters which is most convincingly explained by water-ice deposits. Only for the lunar north pole such shallowing could not be confirmed suggesting (almost) ice-free craters. A study by Schorghofer and Aharonson (2014) shows a mechanism how water-ice can be diffused into the sub-surface in sunlit areas if the maximum and average temperatures stay above 120 K and below 105 K, respectively. Regions offering such conditions can only be found near the lunar poles and cover an area larger than the one occupied by PSRs.

We investigate LEND data in combination with temperature maps. Here, we compile surface and sub-surface temperature maps since the depth to which neutron remote sensing can detect hydrogen is down to ≈ 1 m of planetary regolith (Litvak et al., 2016). We show arguments towards the open question whether or not the identified hydrogen-rich areas in sunlit areas are due to neutron signals stemming from deeper layers where temperatures might be cold enough for water ice to exist.

2 Data and Method

For our study we created high-resolution lunar polar LOLA DTMs (Gläser et al., 2013) centered on the poles. Both DTMs span 650 × 650 km and have an original resolution of 20 m/pixel. The resolution was downsampled to 200 m/pixel to accommodate limitations in computational capabilities. We defined a total of eight regions of interest (RoIs) for which we report illumination and temperature. The RoIs comprise the central 50×50 km subsets of each DTM (see Fig. 1e,2e) as well as regions inside of Cabeus, Haworth and Shoemaker craters at the south pole and nearby Peary, Fibiger and Whipple craters at the north pole. The central regions were chosen due to the extreme illumination conditions found right near the poles which also translate into extreme temperatures, hot and cold. The remaining RoIs were chosen based on studies using data from LEND which identified them as NSRs (Mitrofanov et al., 2012; Sanin et al., 2017). The chosen south polar NSRs correlate (lie within and spread outside) with large, permanently shadowed craters whereas the chosen north polar NSRs conversely lie in warmer non-PSR areas (Boynton et al., 2012; Sanin et al., 2012).

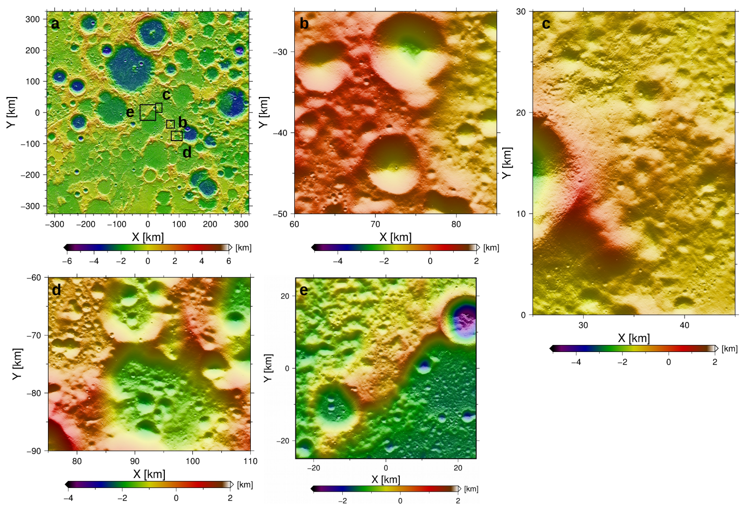

Figure 1. The north polar LOLA DTMs have a resolution of 20 m/pixel. (a) 650 × 650 km north polar DTM with outlines of RoIs. The RoIs are (b) Peary, (c) Whipple, (d) Fibiger craters and (e) the central polar 50 × 50 km region. All maps are displayed in gnomonic map projection and are color-coded by heights. For presentation purposes the map sizes are arbitrary and are not related to each other.

The RoIs are synthetically illuminated (Gläser et al., 2014, 2018) at 12h-increments over a 19-years time frame to cover all seasonal and orbital illumination conditions (note: the lunar precessional cycle lasts 18.6 years). Illumination is derived for each RoI con-

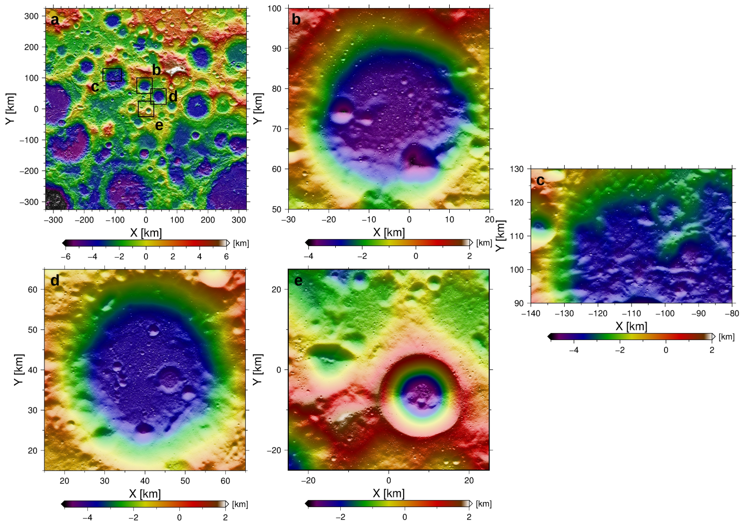

Figure 2. The south polar LOLA DTMs have a resolution of 20 m/pixel. (a) 650 × 650 km south polar DTM with outlines of RoIs. The RoIs are (b) Haworth, (c) Cabeus, (d) Shoemaker craters and (e) the central polar 50 × 50 km region. All maps are displayed in gnomonic map projection and are color-coded by heights. For presentation purposes the map sizes are arbitrary and are not related to each other.

sidering obstructions of the Sun by topography from the respective entire polar 650× 650 km DTM. Note that we treat the Sun as an extended source taking into account the solar-limb darkening effect. At each pixel and time step the instantaneous illumination is used as an input to subsequently solve a one-dimensional representation of the heat equation to model temperatures. In our model (see Gläser and Gläser (2019) for more details) we consider heat conduction in the upper two meters of regolith and derive temperatures for a total of 30 layers, 29 layers in the sub-surface and 1 layer at the surface (compare the first 27 layers given in the first column of Table B1 plus the additional layers at 1.25 m, 1.55 m and 1.85 m). Multiple scattering of reflected sunlight by terrain as well as thermal re-radiation is considered within a window size of 50×50 km. Scattering of sunlight from Earth and thermal re-radiation of an average warm Earth are also considered (Gläser & Gläser, 2019; Trenberth & Stepaniak, 2003). Lastly, heat stemming from nuclear decay in the lunar interior is modeled via a constant radiogenic heat source of 0.016 W/m^2 sitting just below our deepest layer.

3 Results

We started our investigation from a uniform temperature distribution at each of the 30 layers. The surface layer was set to 80 K with temperature declining by 1 K per layer. Hence the deepest layer (30 cm wide and centered at 1.85 m in the sub-surface) started from a uniform temperature distribution of 51K. The DTMs were then illuminated in 12-h time-steps for 19 years in order to cover all effects stemming from the 18.6 years lunar precessional cycle. The chosen time period was January 01, 1991 at midnight to January 1, 2010 at midnight for which roughly the same orbital, seasonal, and hence the same illumination conditions occur at the start and end date. Consequently, we can start to iterate with the last result as our new initial temperature distribution. We found that after five iterations (i.e. 95 a) the largest temperature difference from the forth to the fifth iteration was 0.5 K at the deepest layer and 0.02 K at the surface with average values being one to two orders of magnitude smaller (numbers correspond to the central

RoI at the north pole but are representative for all RoIs presented here). Hence, the solution after the fifth iteration is considered our equilibrated solution from which we derived all results presented in this study. In Fig. 3 the instantaneous illumination and temperature at midnight on January 1, 2010 for the central north polar RoI is displayed at four different depths. While the hottest surface temperatures correspond directly to sunlit areas (Fig. 3c), the sub-surface layers show quite a different temperature distribution. Here, a convolution of many previously conducted temperature patterns is preserved through the low conductivity of the cold upper surface layers and the feasibility of the sub-surface regolith to store heat for longer time-scales, i.e. no direct radiation into space.

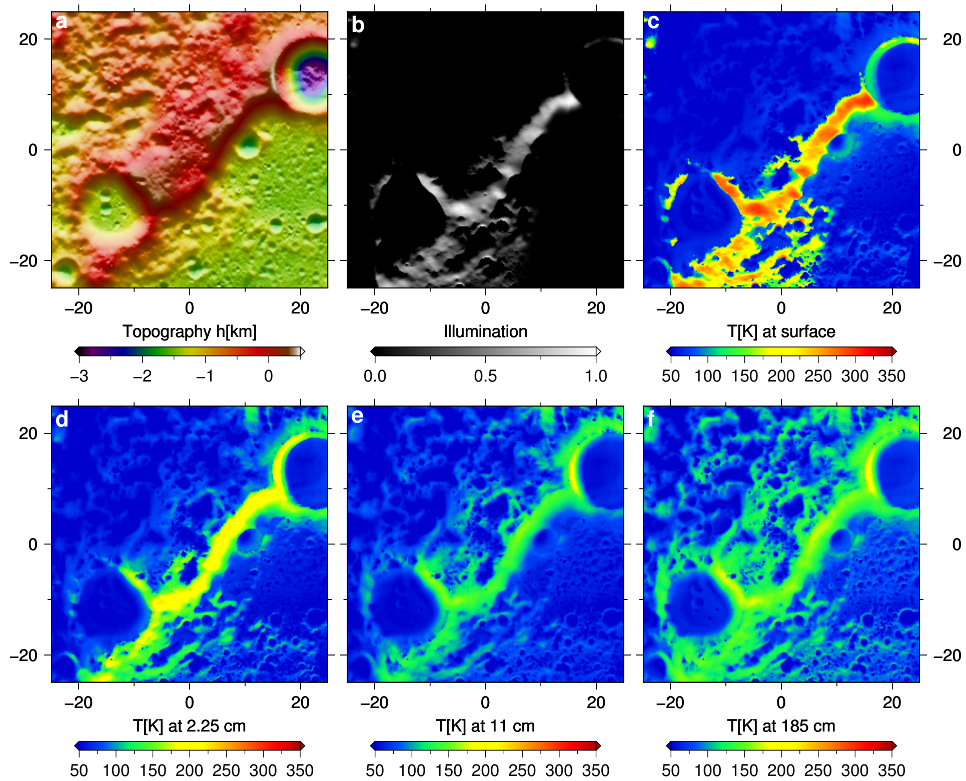

Figure 3. The equilibrated solution (fifth iteration) for the north polar RoI at January 1, 2010 at midnight. (a) The topography of the RoI for context (same as in Fig 1e). (b) Illumination. Temperature at (c) surface, (d) at 2.25 cm depth, (e) at 11 cm depth, (f) at 185 cm depth. Maps are centered at the north pole in gnomonic map projection and are color-coded by (a) heights , (c-f) temperature and (b) gray-scaled and normalized by maximum insolation (444.49 W/m^2).

3.1 Temperature maps

Starting from the equilibrated solutions at each RoI we derived instantaneous, average, depth-to-ice (see section 3.2), minimum and maximum temperature maps over the same 19 years period (see Figs. 4,6). In Fig. 4 we show the maximum temperatures reached within our considered time-frame at four different depths (surface, 2.25 cm, 11 cm and 1.85 m) for the central RoI at the south pole. At surface level the maximum temperatures range here from 23.35 K to 339.07 K and attenuate to 27.91 K to 191.77 K at 185 cm depth, respectively (see Fig. 4c+f). Table 1 lists all minimum, maximum average and maximum temperatures at four selected depths for all eight considered RoIs.

Note that the lowest temperatures at each RoI and depth are identical and are increasing with depth. These static temperature profiles correspond to areas that are permanently and also doubly shadowed regions where the only remaining heat flux is stemming from constantly assumed internal heat sources preventing them from cooling down even further. At these locations no additional fluxes from multiple scattering or Earth shine occur making them the darkest and coldest spots on the Moon. The theoretical minimum temperature of 23.05 K at surface level, neglecting conduction and considering only an internal heat flux of 0.016 W/m^2, is defined by the the Stefan-Boltzmann-Law. Since we have not yet reached the theoretical minimum temperatures with our model (compare Table 1) additional simulation iterations might be necessary to achieve absolute equilibrium. However, the differences are considered marginal, e.g. the maximum theoretical difference is 0.3 K, and as stated before we assume to have an equilibrated solution. Also note that the surface layers are exposed to space and are hence radiating with T^4 according to the Stefan-Boltzmann-Law. Consequently the respective surfaces are cooler than the isolated sub-surface layers.

As expected the highest temperatures occur in the sunlit areas on the surface. Here, temperatures attenuate drastically with depth. Maximum average temperatures are relatively constant through all layers and are virtually identical to the maximum temperature at the lowest surface layer at 1.85 m depth. Here, temperature changes do not occur anymore and temperatures remain constant with respect to diurnal, seasonal and precessional cycles.

		T [K]			
		surface	2.25 cm	11 cm	185 cm
Pole	RoI	Min/Avg/Max	Min/Avg/Max	Min/Avg/Max	Min/Avg/Max
S	central	23.35/184.18/339.07	23.59/187.39/261.20	23.91/187.82/203.66	27.91/191.66/191.77
	Haworth	23.35/182.85/320.82	23.59/193.80/253.88	23.91/194.81/206.88	27.91/198.62/198.65
	Cabeus	23.35/188.70/330.89	23.59/200.97/262.02	23.91/202.10/212.77	27.91/205.89/205.92
	Shoemaker	23.35/184.10/338.26	23.59/188.02/260.89	23.91/189.06/203.24	27.91/192.89/192.93
N	central	23.35/189.35/330.46	23.59/192.38/255.71	23.91/192.86/204.20	27.91/196.70/196.88
	Peary	23.35/180.48/327.22	23.59/192.38/256.75	23.91/193.44/204.43	27.91/197.25/197.32
	Fibiger	23.35/183.54/333.72	23.59/195.18/260.61	23.91/196.30/206.47	27.91/200.08/200.13
	Whipple	23.35/189.34/330.94	23.59/192.38/256.63	23.91/192.86/204.20	27.91/196.69/196.88

Table 1. Minimum, (maximum) average and maximum temperature are presented for eight polar RoIs.

3.2 Depth-to-ice maps

Based on maximum temperature maps of each of our 30 layers (e.g. Fig. 4) depth-to-ice maps can be inferred. For this purpose we stacked all maximum temperature maps and searched from the top to the bottom layer at which depth the temperature dropped below 110 K. We chose this temperature as the limit for the stability of water ice deposits (Killen et al., 1997; Vasavada et al., 1999). From Figs. 4b, 5 we can infer that large areas of the central south polar RoI, e.g. the inside of Shackleton crater, do not receive any direct illumination and classify as PSRs. Here, typical depths at which water ice could be stable are either at surface level or within the upper 1 cm layer, compare Fig. 5. Temperatures at roughly 70 % of the shown area are such that water ice would be stable at depth shallower than 1 m.

Temperature profiles through Shackleton crater, indicated in Fig. 4a,c-f as a black line, are shown in Fig. 6. Here we report the maximum, average and minimum temperatures at our four chosen depth layers. For instance, Fig. 6a shows temperature profiles

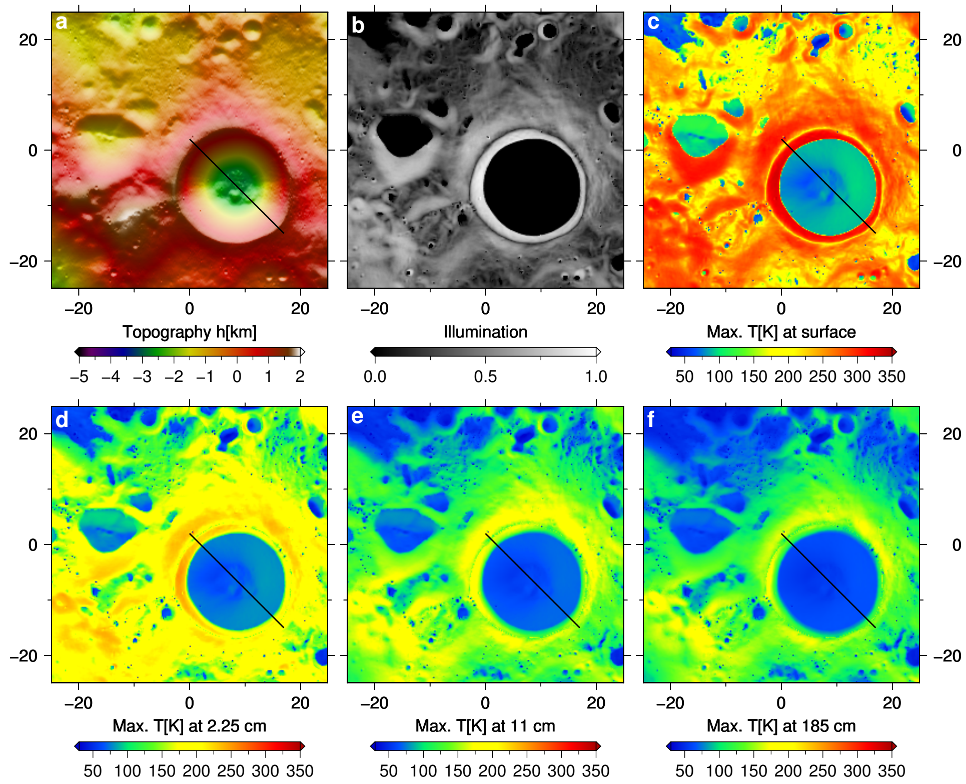

Figure 4. Maximum temperatures reached over the considered time-frame at the central south polar RoI. (a) The topography of the RoI for context. (b) Maximum illumination. Maximum temperature at (c) surface, (d) at 2.25 cm depth, (e) at 11 cm depth and (f) at 185 cm depth. Maps are centered at the south pole in gnomonic map projection and are color-coded by (a) heights, (c-f) temperature and (b) gray-scaled and normalized by maximum insolation (719.53 W/m^2). The black line is the location of the temperature profiles displayed in Fig. 6.

at the surface where the maximum temperature profile (red) reaches temperatures > 300 K outside the PSR and drops to < 100 K inside the PSR. The average (green) and minimum (blue) temperature profiles follow the same trend as the maximum temperature profile but at much lower temperatures with smaller amplitude variations. The topographic profiles (black) are highlighted (cyan) where the maximum temperature is below 110 K indicative for locations where stable water ice could be found. We find that for the larger part of the profile water ice is stable, also at surface level. The temperature profiles slowly converge with increasing depth and at 185 cm depth they are virtually identical, i.e. temperature does not change anymore with the diurnal, seasonal and precessional cycle (see Fig. 6d and Table 1). Between 11 cm and 185 cm depth (Fig. 6b,c) a growing patch of potential water ice can be found right on the crater rim which would be a prime destination for a future landed mission. Generally, locations with extended and continuous periods of illumination are found at the crater rim offering the possibility to charge batteries of rovers and landers relying on solar panels (Gläser et al., 2014, 2018). Hence, rovers with drilling capabilities could reach such potentially water-ice-bearing sites on the rim without traversing down the steep walls of Shackleton crater. Although temperatures would allow for water ice to be stable at a vast area inside the PSR of Shackleton and also at shallow depth on its crater rim, there is no scientific consent whether or not water ice is at all present (e.g. Haruyama et al., 2008; Zuber et al., 2012; Thomson et al., 2012; Haruyama et al., 2013; Spudis et al., 2013).

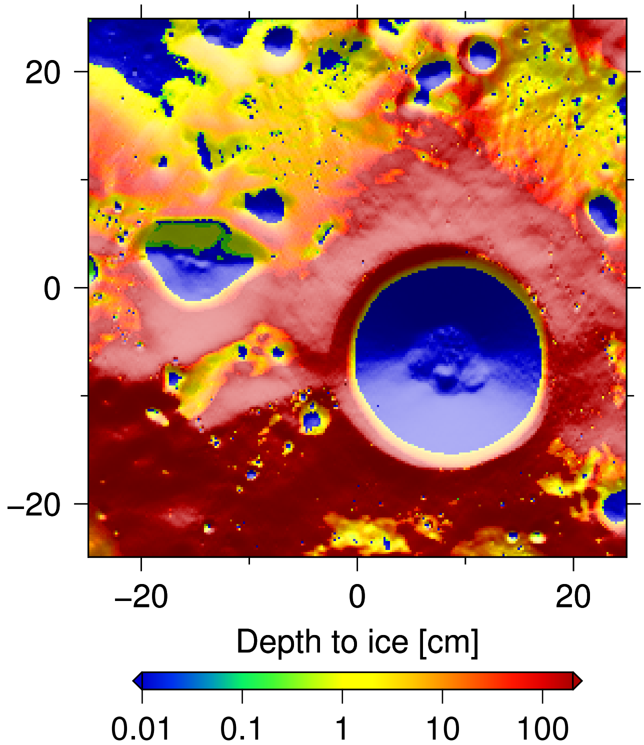

Figure 5. Depth-to-ice (depth at which $T < 110\,\mathrm{K}$) in centimeters for the central south polar RoI derived from 30 stacked maximum temperature maps from surface level down to 185 cm depth. In PSRs potential ice can generally be found at surface level, e.g. Shackleton crater. At 2/3 of the shown area water ice could be stable at depth shallower than 1 m.

3.3 Hydrogen maps

Temperature alone is not compelling evidence in the search for lunar water ice. As a second constraint we incorporate LEND observations. LEND measures the neutron leakage of the Moon allowing the detection of hydrogen present within the upper $\approx 1\,\mathrm{m}$ of regolith (Litvak et al., 2016). Sanin et al. (2017) introduced the suppression parameter ξ which represents the ratio between the average neutron counting within LEND's field-of-view to the average neutron counting of a hydrogen-poor reference area. Maps of the suppression parameter ξ are shown in Fig. 7. Note the 3 selected NSRs at each pole that have distinctively lower counts than their surrounding. Here the lower counts stem from a relatively larger hydrogen abundance, presumably water ice, efficiently moderating the neutron flux. However, the central south polar RoI including Shackleton crater does not show distinct neutron suppression although temperatures would allow for stable surficial water ice (see Figs. 4,5). The central north polar RoI shows faint neutron suppression along the equator-facing rim of Peary crater. However, suppression parameters found outside NSRs are usually $> 10\,\%$ lower, e.g. $\xi \approx 0.8$ inside NSRs and $\xi \approx 0.9$ in areas showing lower neutron counts but were not classified as NSRs.

3.4 Synthesis

If LEND data shows ancient water ice content of the lunar upper $\approx 1\,\mathrm{m}$ of regolith and water ice is stable for geological time-scales at temperatures below 110 K then correlation is expected between (sub-)surface temperature and LEND's neutron count maps and derivatives of it, e.g. neutron suppression maps. Consequently we compared our tem-

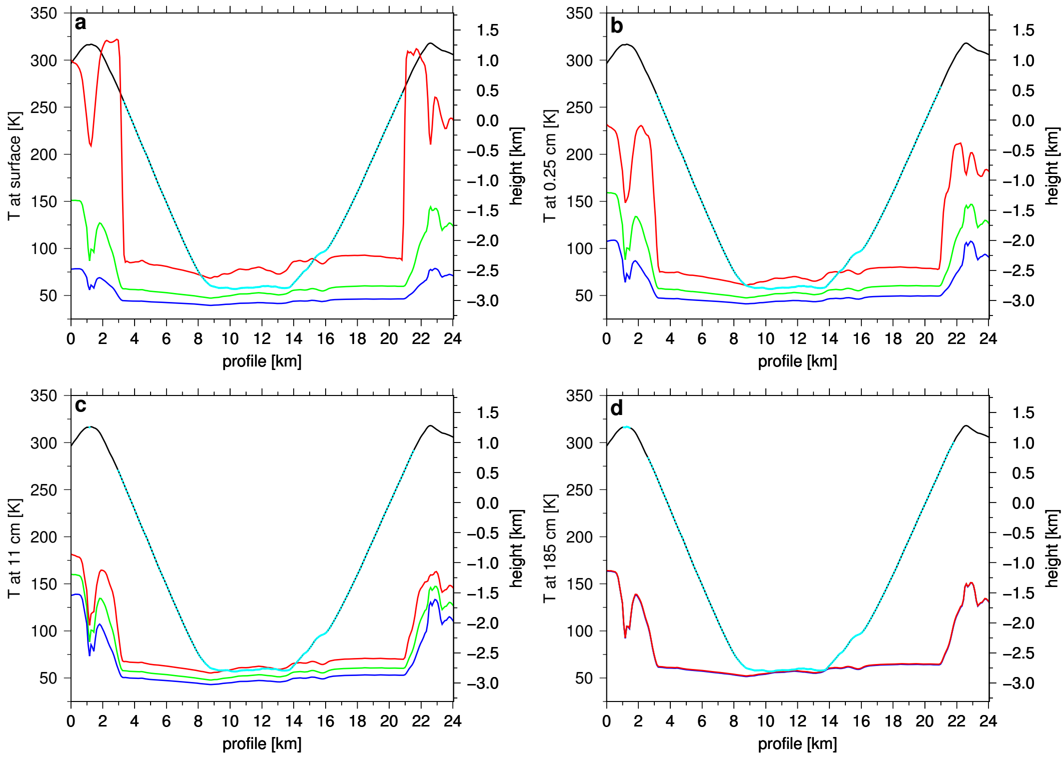

Figure 6. Profile through Shackleton crater as indicated by the black lines in Fig. 4. Each plot shows (black) the topographic profile, (red) maximum temperature profile, (green) average temperature profile, (blue) minimum temperature profile and (cyan) the location on the topographic profile at which water ice can be stable. Profiles correspond to (a) surface, (b) 2.25 cm depth, (c) 11 cm depth and (d) 185 cm depth.

perature maps at each of the 30 layers to LEND neutron suppression maps to reveal the range of depths at which both maps correlate best. Based on the fact that the LCROSS impact site (longitude $-48.7093\,°$, latitude $-84.6796\,°$ (Marshall et al., 2011)) at which water ice concentrations of $\approx 5.6 \pm 2.9\,\%$ by mass (Colaprete et al., 2010) were found lies in a region of suppression parameters $\xi <= 0.83$, we define this value as a clear sign of water ice (see Fig.A5). The model by Sanin et al. (2017) suggests that a suppression parameter of $\xi = 0.83$ corresponds to $0.37\,\%$ by mass of water uniformly distributed in the subsurface soil. They also show that by increasing the thickness of the dry top layer and placing the ice uniformly below it, the water ice concentrations of $\approx 5.6 \pm 2.9\,\%$ by mass measured by LCROSS can be reproduced.

For our analysis we derived maximum temperatures over the 19 year period and mapped possible water ice locations based on temperature (where $T <= 110\,\mathrm{K}$) and on neutron suppression parameters (where $\xi <= 0.83$) at four different depths for our eight polar RoIs (see Figs. A1-A8). We chose to display depth layers at surface level, 2.25 cm, 11 cm and 95 cm depth up to which LEND is able to detect the presence of hydrogen. The central polar RoIs which are not classified as NSRs are shown in Figs. A1,A2. The three chosen south polar NSRs can be labeled as 'classical' NSRs; they reside within the PSRs of large, cold crater floors, see Fig. A3-A5. Our three north polar NSRs, however, can be labeled as atypical since they are all found in non-PSR areas, see Fig. A6-A8.

At each site and depth layer we also determined the overlap of areas which define potential water ice reservoirs, either by temperature ($T <= 110\,\mathrm{K}$) or by suppression

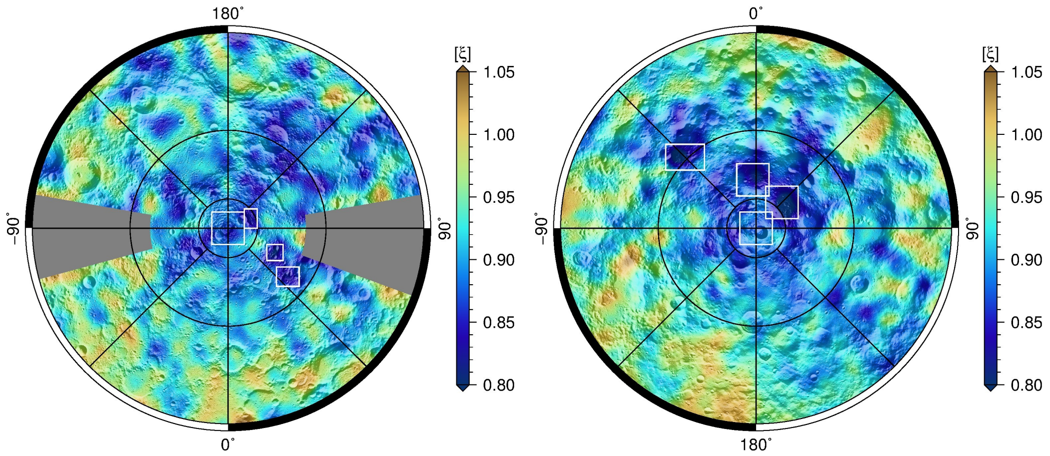

Figure 7. Maps of suppression parameter ξ derived from neutron counts measured by LEND. RoIs are shown within white boxes. (left) North polar map of ξ with the central RoI and three NSRs denoted as Fibiger, Whipple and Peary. The gray areas are left out due to poor statics of neutron measurements in these regions (see Sanin et al. (2017)). (right) South polar map of ξ with the central RoI and three NSRs denoted as Cabeus, Haworth and Shoemaker.

parameter ($\xi <= 0.83$). As we have no information at which depth or range of depths the suppression parameter is prevalent, i.e. where the hydrogen reservoir is located, we want to constrain those boundaries with our study. For this purpose we derived growth rates for the fraction of the overlapping areas of potential water ice with increasing depth (Fig. 8). We defined that if the overlapping fraction grows less than 0.1 %/cm with increasing depth then we consider to have found the lower boundary of the suppression region.

For the south polar NSRs it is noticeable that large parts of the areas confined by the contour lines of $T = 110\,\mathrm{K}$ and $\xi = 0.83$ are coincident at surface level already (see also Table B1). Especially at Haworth crater the strong hydrogen signal is completely within the contour lines of $T = 110\,\mathrm{K}$, which we interpret as evidence for (near-)surficial water ice. Here, deeper layers might not add a significant contribution to the observed LEND signal. At Shoemaker crater, areas confined by the contour lines of $T = 110\,\mathrm{K}$ and $\xi = 0.83$ at surface level overlap 72.4 % (see Table B1) but there is still a strong hydrogen signal where surface temperatures are too hot. At 11 cm depth the area within the $T = 110\,\mathrm{K}$ contour line matches well with the area confined by the $\xi = 0.83$ contour line, indicative for LEND's observed hydrogen signal stemming from the top $\approx$ 10–20 cm layers of regolith, including the surface itself. In fact, we find that below 19 cm depth the overlapping area of the neutron suppression region $\xi <= 0.83$ and cold temperatures $T <= 110\,\mathrm{K}$ has reached 95.56 % (see Table B1). Here, at greater depths the overlap does not significantly grow any further, i.e. the growth rate drops below our chosen limit of 0.1 %/cm (see Fig. 8b). At Cabeus crater, for which we definitely know that water ice is present, we find a good match between the areas confined by contour lines of $T = 110\,\mathrm{K}$ and $\xi = 0.83$ at surface level and also at 2.25 cm depth (see Fig. A5). Here we find that growth rates are marginal below depths of 11 cm where the overlap reaches 98.51 % (see Table B1). Based on these results we suggest that water ice is already present within the upper $\approx$ 10 cm at Cabeus crater.

For the atypical NSRs at the north pole we encounter a vastly different scenario. As mentioned before the NSRs reside in non-PSR areas and their existence and development is much harder to explain. In general the suppression parameter ξ is fainter than

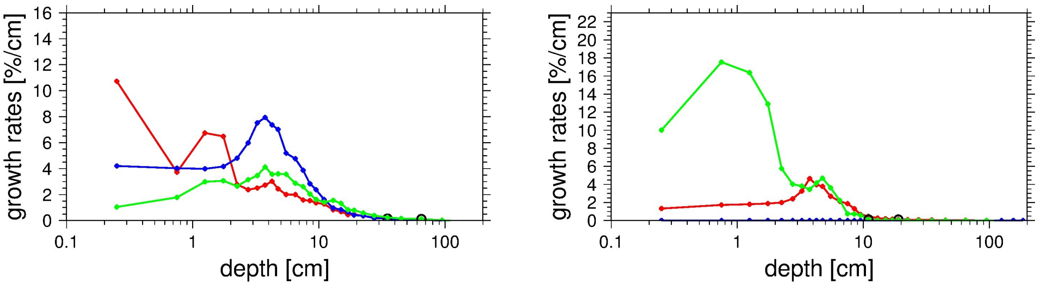

Figure 8. Growth rates in %/cm of the overlapped fraction of NSRs by layers of cold temperatures ($T < 110\,\mathrm{K}$). Left: north polar craters Peary (red), Fibiger (blue) and Whipple (green). Right: south polar craters Shoemaker (red), Haworth (blue) and Cabeus (green). The atypical NSRs at the north pole continue to grow their overlapped area with cold layers in depths below 10 cm. For the classical NSRs at the south pole growth rates decrease quickly below depths of $\approx 4\,\mathrm{cm}$. Note the excessive growth rates of Cabeus in the first 2 cm where the absolute overlap grows by $\approx 30\,\%$.

for the three pronounced south polar NSRs. Further there is a complete lack of correlation of the areas confined by the contour lines of $T = 110\,\mathrm{K}$ and $\xi = 0.83$ at surface level, as was expected due to occasional direct illumination. For instance, the overlap of the contoured areas at surface level lie between 5.56−10.62 % in contrast to 52.49−100 % at the south polar NSRs (see Table B1). For the NSRs near Whipple and Fibiger crater the first layer at which areas with temperatures at $T = 110\,\mathrm{K}$ that visually overlap with the suppression region occur at 11 cm depth, see Figs. A6c,A7c. Growth rates continue but are low towards the deepest layer at 95 cm depth (see Fig. 8a). As LEND can measure down to such depths the observed signal could be explained by the existence of water ice residing between these depth layers. From growth rates we find that at 65 cm depth at Whipple and 35 cm depth at Fibiger crater growth ceases at overlaps of 52.55 % and 67.28 %, respectively. Similarily, the NSR just outside Peary crater does show some near-surface temperature patterns at 11 cm depth (Fig. A8b) that could explain parts of the LEND signal but lower layers, e.g. at 95 cm depth can explain the observed signal slightly better. For Peary we find that growth rates cease at a depth of 35 cm where a total overlap of 47.44 % is reached. This represents the lowest percentage in overlap of all six evaluated NSRs. Although we find correlations between suppression regions and cold temperature layers at the north polar NSRs, the results are not as convincing as for the south polar NSRs and the signal also seems to stem from wider and deeper layers, i.e. upper $\approx 35 - 65\,\mathrm{cm}$ in contrast to upper $\approx 0 - 19\,\mathrm{cm}$ for the south polar NSRs.

Note, that we also produced temperature maps for even greater depths despite LEND's inability to detect water from deeper layers than 1 m. It was found that the emerging temperature patterns do not differ significantly from the maps at 95 cm depth and would therefore not offer a better explanation for the shape and location of the NSRs. Further we showed that growth rates for the overlap of all NSRs with cold temperature layers cease above 1 m depth (see Table B1).

Although the central polar regions both offer large areas with temperatures below 110 K we find no significant neutron suppression and hence no sign for water ice (see Figs. A1,A2).

4 Discussion

The co-evaluation of LEND's suppression parameters with temperature clearly supports the existence of (near-)surface water ice at our selected south polar NSRs. Here, the 'classical' theory of how wet PSRs come into existence seems to hold; water molecules migrate via ballistic hops (Butler et al., 1993; Butler, 1997) from anywhere on the lunar surface towards the poles and accumulate on the cold surfaces within PSRs (Watson et al., 1961). From growth rates in Fig. 8 we conclude that ice at the NSRs of Shoemaker and Cabeus is mostly concentrated within the upper 4 cm after which growth rates sharply decreases and ceases at 19 cm. Most impressively is the absolute growth of 30 % in overlap at Cabeus crater within the top 2 cm depth (see Fig. 8 and Table B1). The NSR within the PSR of Haworth crater suggests water ice is present at surface level. However we know from previous studies (e.g. Mitrofanov et al., 2012) that not all PSRs in return are NSRs, i.e. host significant amount of water ice.

For our north polar NSRs the accumulation mechanism must differ from the south polar NSRs since here surface temperatures are too high for water ice to become trapped. We further note that our selected NSRs all reside on relatively warmer equator-facing slopes at which generally no water ice is found (Rubanenko et al., 2019). Nevertheless LEND shows a clear sign of water at those sites and we could show with this study that temperatures in the near sub-surface are such that water ice can be stable. One plausible scenario would be that water molecules at those locations are efficiently buried. In accordance we find that growth rates remain active to greater depths than at the south polar NSRs (see Fig. 8). Interestingly, growth rates also decrease beyond a similar depth as reported for the south pole, i.e. 4 cm, suggesting that favorable temperatures for water ice are generally found within the top few centimeters. However, the decrease in growth rates is significantly slower than at the south pole and growth continues to depths of up to 65 cm. In fact, Schorghofer and Aharonson (2014) found that water molecules can be pumped down into the sub-surface by diurnal temperature cycles under very specific circumstances. They found that ideal conditions for pumping emerge if the mean surface temperature is below 105 K and the maximum surface temperature is above 120 K. Although they report that such temperature regimes are commonly found on pole-facing slopes they also found that within a few degrees of the poles pumping is actually preferred on equator-facing slopes. As stated before, our selected north polar NSRs all reside on equator-facing slopes within a few degrees of the poles and we find that $\approx 40-60\,\%$ of the surface area confined by the suppression parameter ($\xi <= 0.83$) do indeed offer such ideal pumping conditions. Since the areas where ice pumping occur complement the areas where water ice can be stable, i.e. the areas do not overlap, the total surface area of the NSRs for which we can either find stable water ice or find ice pumping amounts to $\approx 45-70\,\%$. Those numbers are found again at 65 cm depth where we defined the lower boundary for water ice by ceasing growth rates (compare to Table B1). Note that the ice pump is inactive below ≈ 20 cm and lower layers of ice need to be buried by a different mechanism, e.g. mass wasting event. We note that this mechanism is also active at the south polar NSRs at the smaller fractions where the NSRs are occasionally in sunlight, e.g. Shoemaker and Cabeus crater (see Fig. A3, A5). Here the total percentage of NSR overlap at the surface, either with temperature or ice pumping, amounts to $\approx 98-100\,\%$. Similar values are again found at our defined lower boundaries for water ice (compare to Table B1).

5 Conclusion

This study confirms previous observations that temperature alone is not a sufficient predictor of the distribution of ice deposits. For instance, we showed that water ice locations predicted solely by maximum temperature do not always coincide with NSRs identified by LEND, insinuating that maximum temperature might not be the only or main driver for the accumulation of water ice. Further there is a significant difference in the locations where NSRs are found at each pole. Our selected south polar NSRs all follow the 'classical' view that water ice only accumulates in the cold, polar PSRs. Our selected north polar NSRs drastically differ in that none of them are found in a PSR. Although we can show that their existence can be described by ice pumping and subsequent accumulation at cold layers in the sub-surface, it is unclear why the polar regions differ in such way. We suspect that the accumulation process of water ice in just some of the south polar PSRs and in generally not in north polar PSRs seems to stem from an unconnected and local rather than an ubiquitous and global process since the thermal environment is comparable in all polar PSRs.

Although temperature cannot point to water ice reservoirs alone it is an essential pre-condition for water ice and always needs to be evaluated to support other observations. In conclusion we could show that the six NSRs investigated in this study coincide with temperature maps which allow for water ice or ice pumping, either at surface level or within the first meter of regolith.

409 ## Appendix A Figures

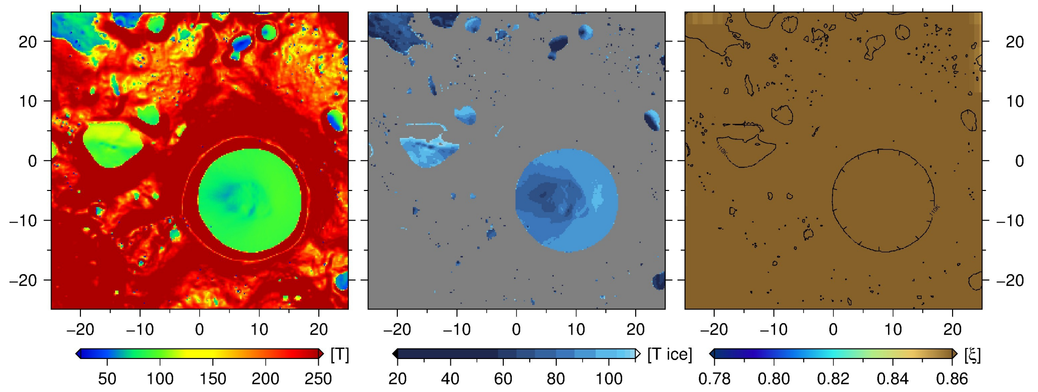

Figure A1. Central south polar RoI. (Left) Maximum temperature. (Middle) Possible locations for water ice ($T <= 110\,\mathrm{K}$) and (right) LEND neutron suppression parameter map at surface level. The areas where $T <= 110\,\mathrm{K}$ are contoured in black, however, no significant neutron suppression can be found (i.e. $\xi <= 0.83$).

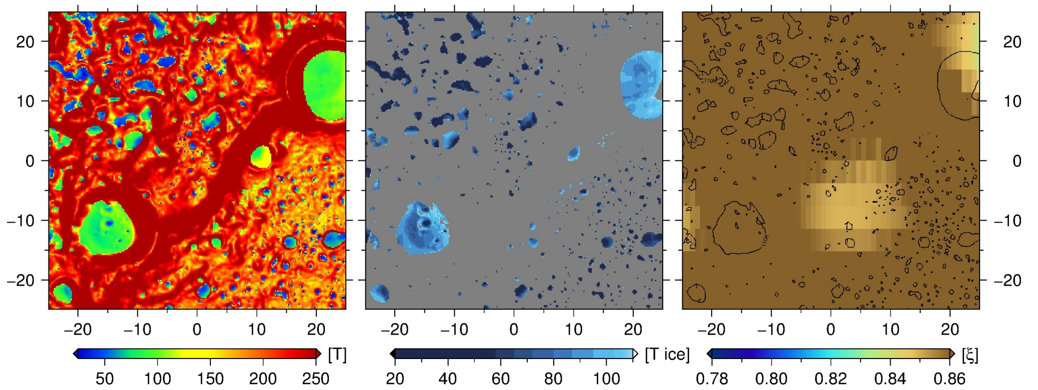

Figure A2. Central north polar RoI. (Left) Maximum temperature. (Middle) Possible locations for water ice ($T <= 110\,\mathrm{K}$) and (right) LEND neutron suppression parameter map at surface level. The areas where $T <= 110\,\mathrm{K}$ are contoured in black, however, no significant neutron suppression can be found (i.e. $\xi <= 0.83$).

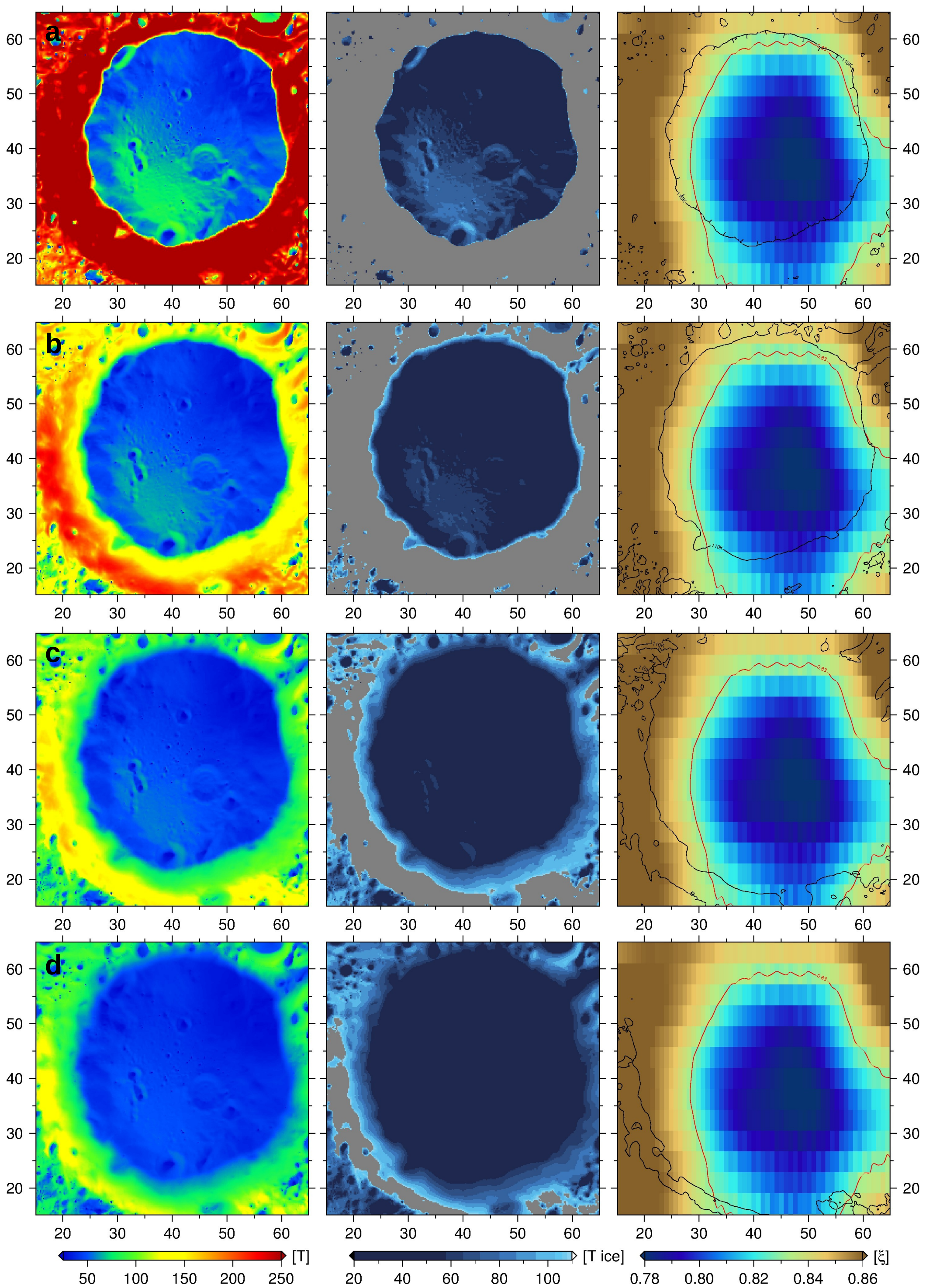

Figure A3. South polar crater Shoemaker. (Left) Maximum temperature. (Middle) Possible locations for water ice ($T <= 110\,\mathrm{K}$) and (right) LEND neutron suppression parameter map at (a) surface level, (b) 2.25 cm, (c) 11 cm and (d) 95 cm. The areas where $T <= 110\,\mathrm{K}$ and $\xi <= 0.83$ are contoured in black and red, respectively.

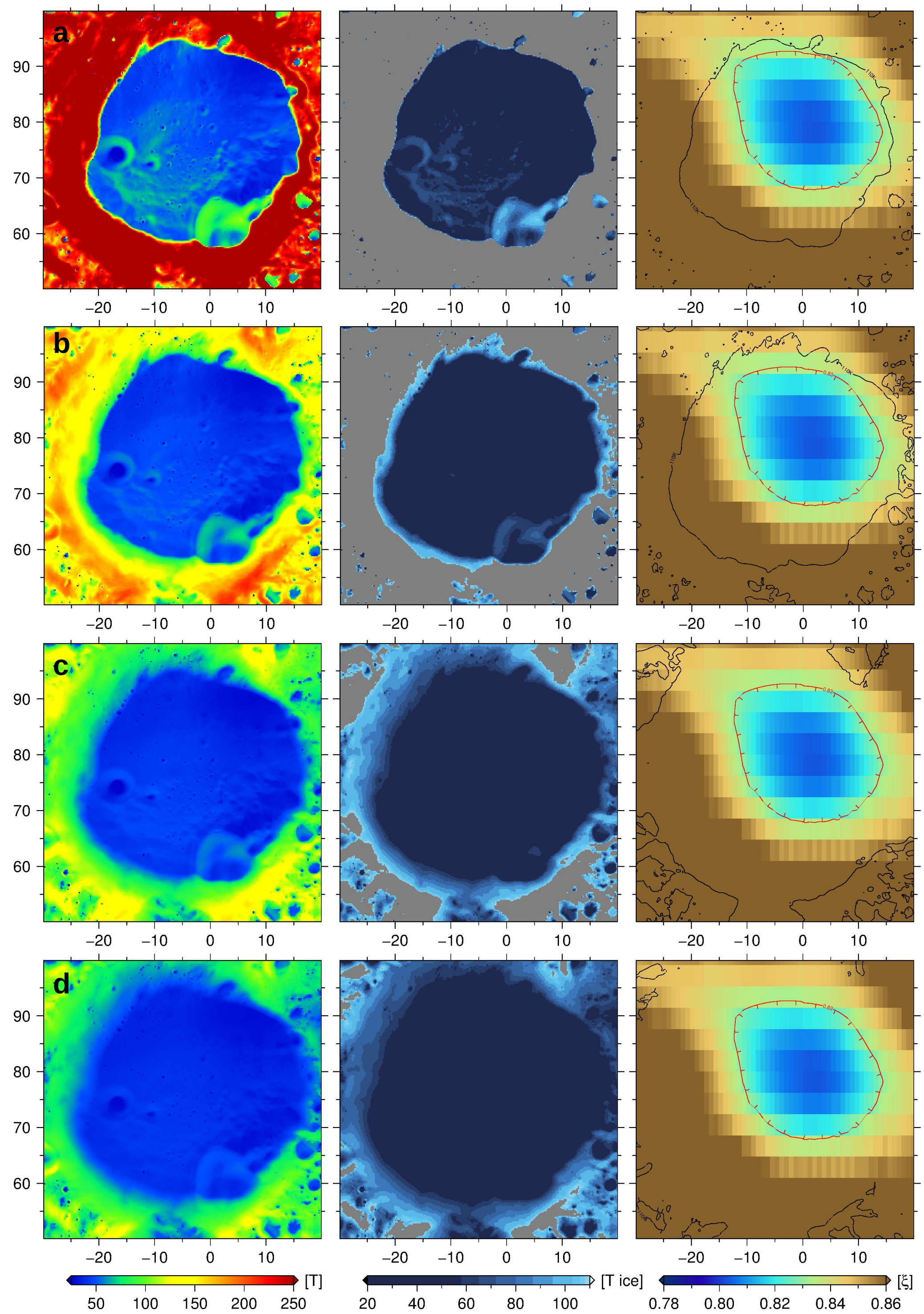

Figure A4. South polar crater Haworth. (Left) Maximum temperature. (Middle) Possible locations for water ice ($T <= 110\,\mathrm{K}$) and (right) LEND neutron suppression parameter map at (a) surface level, (b) 2.25 cm, (c) 11 cm and (d) 95 cm. The areas where $T <= 110\,\mathrm{K}$ and $\xi <= 0.83$ are contoured in black and red, respectively.

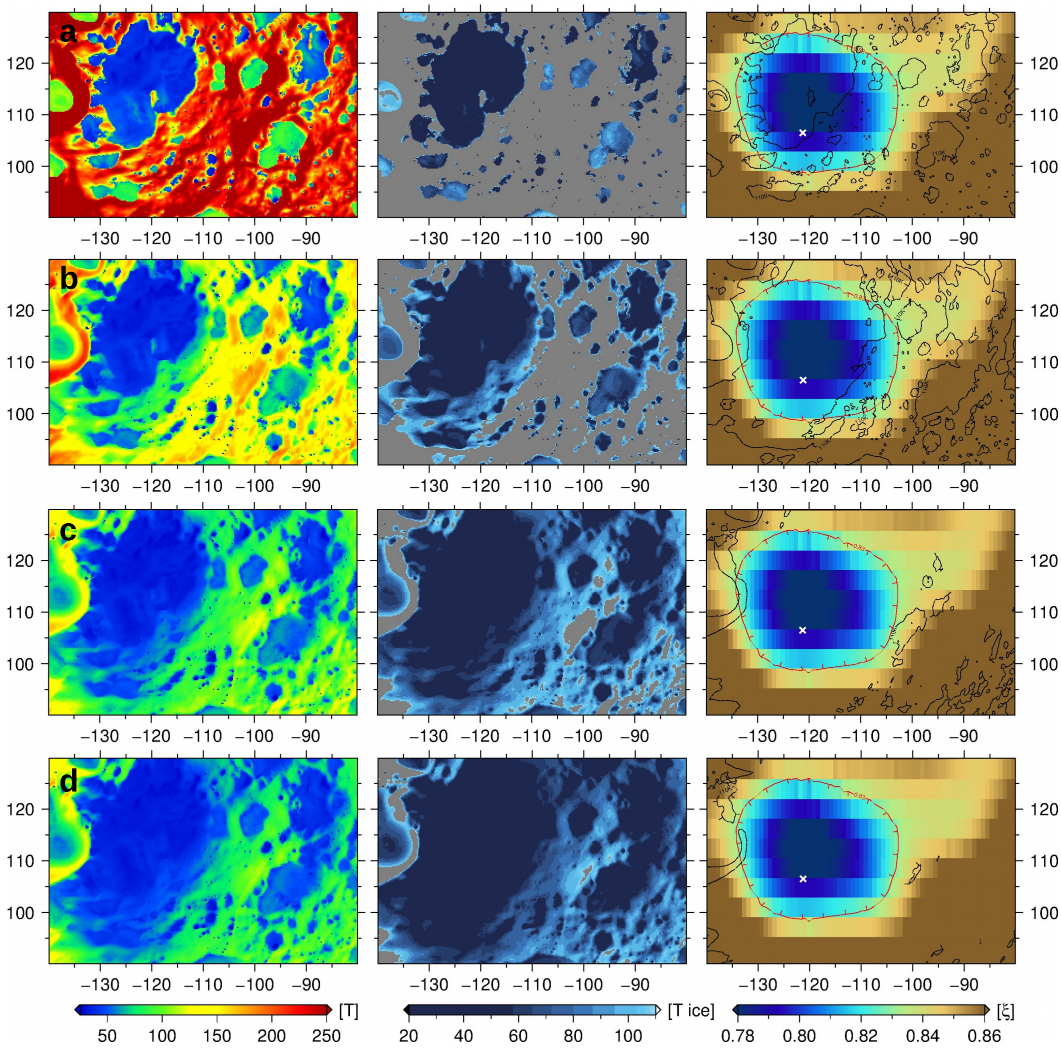

Figure A5. South polar crater Cabeus. The LCROSS impact site is indicated by a white cross. (Left) Maximum temperature. (Middle) Possible locations for water ice ($T <= 110$ K) and (right) LEND neutron suppression parameter map at (a) surface level, (b) 2.25 cm, (c) 11 cm and (d) 95 cm. The areas where $T <= 110$ K and $\xi <= 0.83$ are contoured in black and red, respectively.

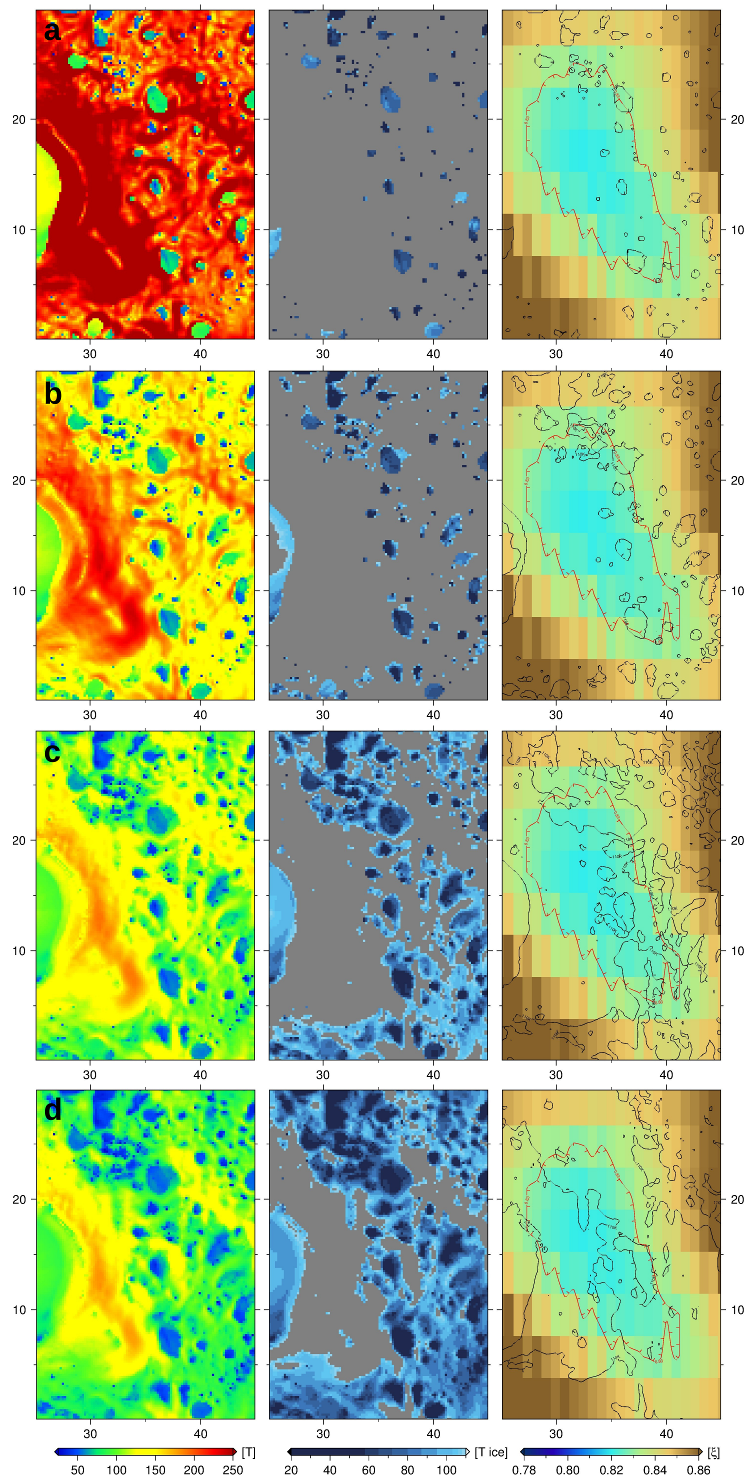

Figure A6. Area outsides north polar crater Whipple. (Left) Maximum temperature. (Middle) Possible locations for water ice ($T <= 110\,\mathrm{K}$) and (right) LEND neutron suppression parameter map at (a) surface level, (b) 2.25 cm, (c) 11 cm and (d) 95 cm. The areas where $T <= 110\,\mathrm{K}$ and $\xi <= 0.83$ are contoured in black and red, respectively.

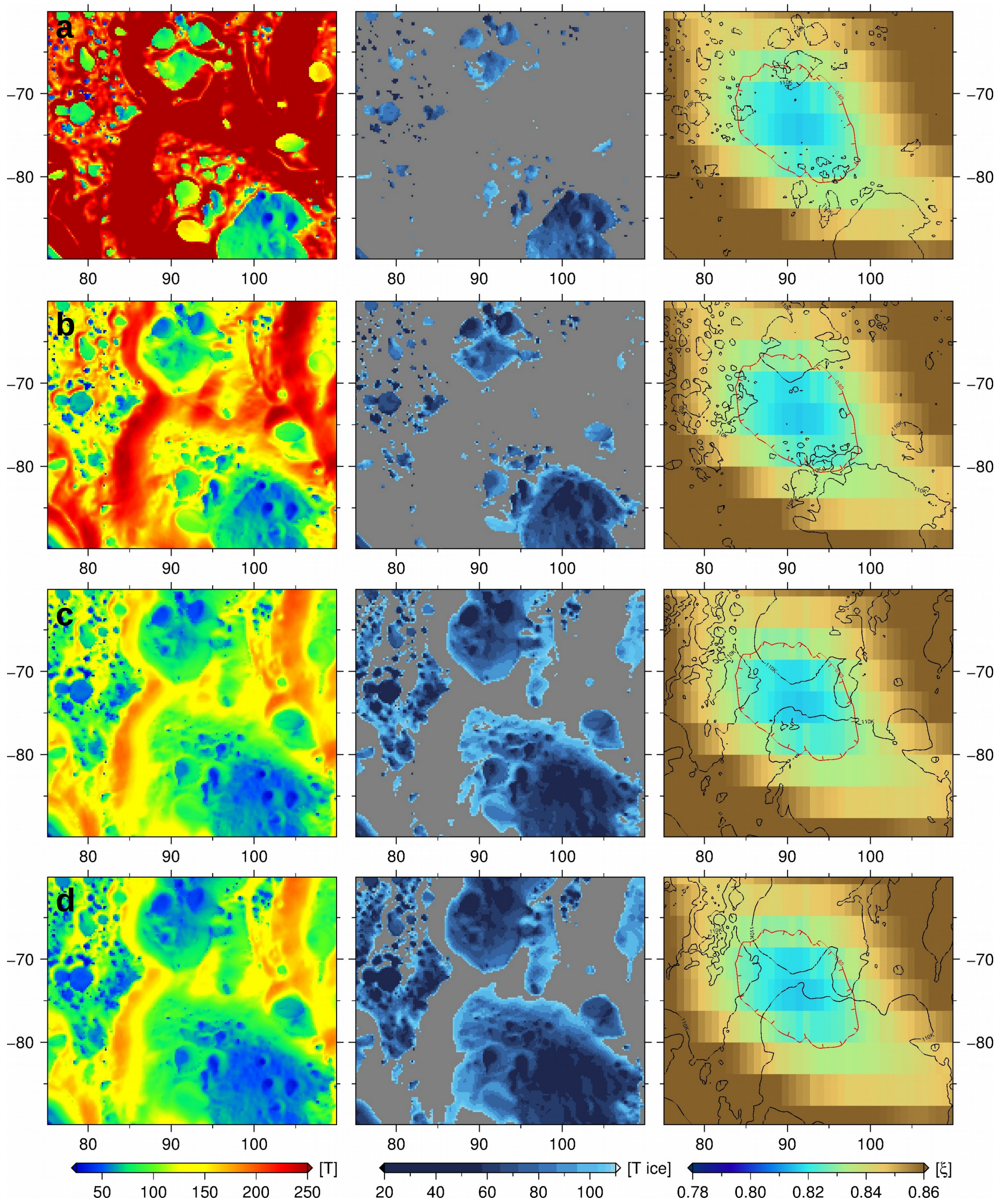

Figure A7. Area outsides north polar crater Fibiger. (Left) Maximum temperature. (Middle) Possible locations for water ice ($T <= 110\,\mathrm{K}$) and (right) LEND neutron suppression parameter map at (a) surface level, (b) 2.25 cm, (c) 11 cm and (d) 95 cm. The areas where $T <= 110\,\mathrm{K}$ and $\xi <= 0.83$ are contoured in black and red, respectively.

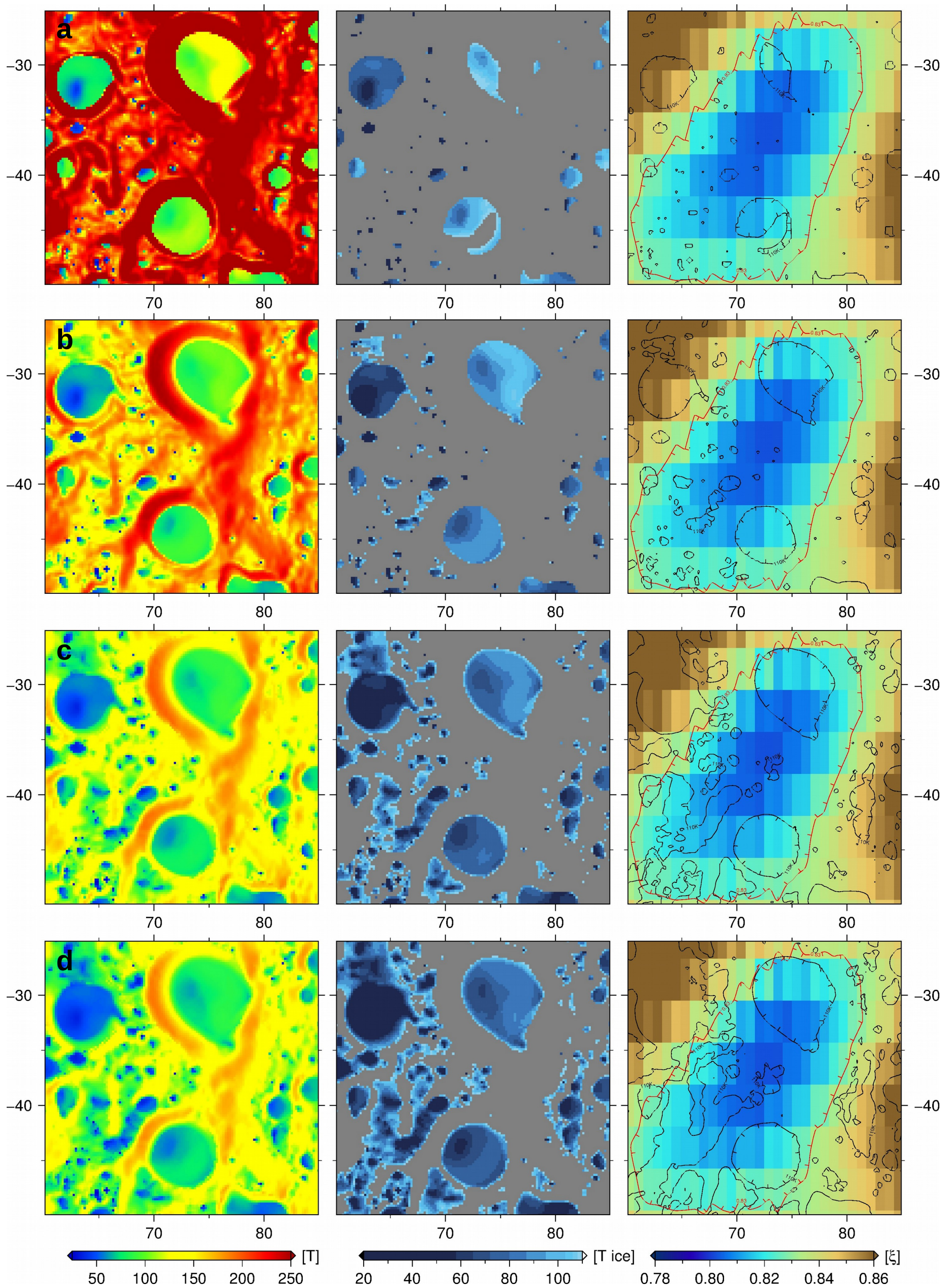

Figure A8. Area outsides north polar crater Peary. (Left) Maximum temperature. (Middle) Possible locations for water ice (T <= 110 K) and (right) LEND neutron suppression parameter map at (a) surface level, (b) 2.25 cm, (c) 11 cm and (d) 95 cm. The areas where T <= 110 K and ξ <= 0.83 are contoured in black and red, respectively.

Appendix B Table

	Overlap in % of NSRs with cold layers ($T <= 110\,\mathrm{K}$) at					
	south pole			north pole		
Depth [cm]	Shoemaker	Haworth	Cabeus	Whipple	Fibiger	Peary
0.0000	72.40	**100.00**	52.49	5.56	10.62	9.88
0.2500	72.73	100.00	54.99	5.82	11.67	12.56
0.7500	73.59	100.00	63.76	6.71	13.68	14.42
1.2500	74.49	100.00	71.95	8.20	15.67	17.79
1.7500	75.43	100.00	78.40	9.73	17.75	21.03
2.2500	76.43	100.00	81.27	11.05	20.15	22.42
2.7500	77.63	100.00	83.28	12.62	23.14	23.61
3.2500	79.26	100.00	85.19	14.35	26.90	24.86
3.7500	81.58	100.00	86.91	16.41	30.87	26.22
4.2500	83.56	100.00	88.99	18.19	34.55	27.73
4.7500	85.45	100.00	91.33	19.99	38.06	28.95
5.5000	87.46	100.00	94.05	22.66	41.95	30.45
6.5000	89.58	100.00	96.28	25.53	46.71	32.45
7.5000	91.45	100.00	97.02	28.14	50.58	34.03
8.5000	92.75	100.00	97.74	30.18	53.41	35.56
9.5000	93.42	100.00	98.33	31.80	55.78	36.92
11.0000	94.10	100.00	**98.51**	33.91	58.21	38.83
13.0000	94.65	100.00	98.57	37.01	60.14	40.48
15.0000	95.03	100.00	98.68	39.65	61.81	41.85
17.0000	95.32	100.00	98.73	41.30	63.13	42.76
19.0000	**95.56**	100.00	98.82	42.88	63.95	43.74
22.5000	95.90	100.00	98.86	44.91	65.24	44.97
27.5000	96.34	100.00	98.88	46.81	66.17	46.11
35.0000	96.79	100.00	98.91	48.62	**67.28**	**47.29**
45.0000	97.19	100.00	98.96	50.09	67.97	48.00
65.0000	97.74	100.00	99.03	**52.55**	69.03	48.89
95.0000	98.05	100.00	99.04	53.09	69.13	49.01

Table B1. Overlap of LEND suppression regions of $\xi <= 0.83$ and areas with temperatures $T <= 110\,\mathrm{K}$ given in percentages. For the south polar NSRs growth rates cease ($g < 0.1\,\%/\mathrm{cm}$) within the upper 19 cm. At the north polar NSRs growth rates continue up to depths of 65 cm, i.e. at least three-times deeper than at the south polar NSRs. The depths at which growth rates cease at each site are presented in bold.

Acknowledgments

P. Gläser was funded by a Grant of the German Research Foundation (GL 865/2-1). We gratefully acknowledge the support of NVIDIA Corporation with the donation of a Quadro P6000 GPU used for this research. Last, we wish to thank the LRO Science Teams for releasing such wonderful data products. The data to reproduce figures and results presented in this study can be accessed online at `http://dx.doi.org/10.14279/depositonce-10363`.

References

Arnold, J. R. (1979, September). Ice in the lunar polar regions. *Journal of Geophysical Research*, *84*, 5659-5668. doi: 10.1029/JB084iB10p05659

Benna, M., Hurley, D. M., Stubbs, T. J., Mahaffy, P. R., & Elphic, R. C. (2019, April). Lunar soil hydration constrained by exospheric water liberated by meteoroid impacts. *Nature Geoscience*, *12*(5), 333-338. doi: 10.1038/s41561-019-0345-3

Boynton, W. V., Droege, G. F., Mitrofanov, I. G., McClanahan, T. P., Sanin, A. B., Litvak, M. L., . . . Starr, R. (2012, December). High spatial resolution studies of epithermal neutron emission from the lunar poles: Constraints on hydrogen mobility. *Journal of Geophysical Research (Planets)*, *117*, E00H33. doi: 10.1029/2011JE003979

Bussey, D. B. J., McGovern, J. A., Spudis, P. D., Neish, C. D., Noda, H., Ishihara, Y., & Sørensen, S.-A. (2010, August). Illumination conditions of the south pole of the Moon derived using Kaguya topography. *Icarus*, *208*, 558-564. doi: 10.1016/j.icarus.2010.03.028

Butler, B. J. (1997). The migration of volatiles on the surfaces of mercury and the moon. *Journal of Geophysical Research: Planets*, *102*(E8), 19283-19291. Retrieved from `https://agupubs.onlinelibrary.wiley.com/doi/abs/10.1029/97JE01347` doi: 10.1029/97JE01347

Butler, B. J., Muhleman, D. O., & Slade, M. A. (1993). Mercury: full-disk radar images and the detection and stability of ice at the north pole. *Journal of Geophysical Research: Planets*, *98*(E8), 15003-15023. Retrieved from `https://agupubs.onlinelibrary.wiley.com/doi/abs/10.1029/93JE01581` doi: 10.1029/93JE01581

Clark, R. N. (2009, October). Detection of Adsorbed Water and Hydroxyl on the Moon. *Science*, *326*(5952), 562. doi: 10.1126/science.1178105

Colaprete, A., Schultz, P., Heldmann, J., Wooden, D., Shirley, M., Ennico, K., . . . Sollitt, L. (2010). Detection of water in the lcross ejecta plume. *Science*, *330*(6003), 463–468. Retrieved from `https://science.sciencemag.org/content/330/6003/463` doi: 10.1126/science.1186986

Crider, D., & Vondrak, R. (2002). Hydrogen migration to the lunar poles by solar wind bombardment of the moon. *Advances in Space Research*, *30*(8), 1869 - 1874. Retrieved from `http://www.sciencedirect.com/science/article/pii/S0273117702004933` doi: https://doi.org/10.1016/S0273-1177(02)00493-3

Feldman, W. C., Maurice, S., Binder, A. B., Barraclough, B. L., Elphic, R. C., & Lawrence, D. J. (1998, September). Fluxes of Fast and Epithermal Neutrons from Lunar Prospector: Evidence for Water Ice at the Lunar Poles. *Science*, *281*, 1496. doi: 10.1126/science.281.5382.1496

Gläser, P., & Gläser, D. (2019, Jul). Modeling near-surface temperatures of airless bodies with application to the Moon. *Astronomy & Astrophysics*, *627*, A129. doi: 10.1051/0004-6361/201935514

Gläser, P., Haase, I., Oberst, J., & Neumann, G. A. (2013, Dec). Co-registration of laser altimeter tracks with digital terrain models and applications in planetary science. *Planetary and Space Science*, *89*, 111-117. doi: 10.1016/j.pss.2013.09.012

Gläser, P., Oberst, J., Neumann, G. A., Mazarico, E., Speyerer, E. J., & Robinson, M. S. (2018, Nov). Illumination conditions at the lunar poles: Implications for future exploration. *Planetary and Space Science*, *162*, 170-178. doi: 10.1016/j.pss.2017.07.006

Gläser, P., Scholten, F., De Rosa, D., Marco Figuera, R., Oberst, J., Mazarico, E., . . . Robinson, M. S. (2014, Nov). Illumination conditions at the lunar south pole using high resolution Digital Terrain Models from LOLA. *Icarus*, *243*, 78-90. doi: 10.1016/j.icarus.2014.08.013

Haruyama, J., Ohtake, M., Matsunaga, T., Morota, T., Honda, C., Yokota, Y., . . . Josset, J.-L. (2008, Nov). Lack of Exposed Ice Inside Lunar South Pole Shackleton Crater. *Science*, *322*(5903), 938. doi: 10.1126/science.1164020

Haruyama, J., Yamamoto, S., Yokota, Y., Ohtake, M., & Matsunaga, T. (2013, Aug). An explanation of bright areas inside Shackleton Crater at the Lunar South Pole other than water-ice deposits. *Geophysical Research Letters*, *40*(15), 3814-3818. doi: 10.1002/grl.50753

Killen, R. M., Benkhoff, J., & Morgan, T. H. (1997, January). Mercury's Polar Caps and the Generation of an OH Exosphere. *Icarus*, *125*(1), 195-211. doi: 10.1006/icar.1996.5601

Litvak, M. L., Mitrofanov, I. G., Sanin, A. B., Bakhtin, B. N., Bodnarik, J. G., Boynton, W. V., ... Starr, R. (2016, Mar). The variations of neutron component of lunar radiation background from LEND/LRO observations. *Planetary and Space Science*, *122*, 53-65. doi: 10.1016/j.pss.2016.01.006

Marshall, W., Shirley, M., Moratto, Z., Colaprete, A., Neumann, G., Smith, D., ... et al. (2011, May). Locating the lcross impact craters. *Space Science Reviews*, *167*(1-4), 7192. Retrieved from `http://dx.doi.org/10.1007/s11214-011-9765-0` doi: 10.1007/s11214-011-9765-0

Mazarico, E., Neumann, G. A., Smith, D. E., Zuber, M. T., & Torrence, M. H. (2011, February). Illumination conditions of the lunar polar regions using LOLA topography. *Icarus*, *211*, 1066-1081. doi: 10.1016/j.icarus.2010.10.030

Mitrofanov, I., Litvak, M., Sanin, A., Malakhov, A., Golovin, D., Boynton, W., ... Vostrukhin, A. (2012, Jul). Testing polar spots of water-rich permafrost on the Moon: LEND observations onboard LRO. *Journal of Geophysical Research (Planets)*, *117*, E00H27. doi: 10.1029/2011JE003956

Mitrofanov, I., Sanin, A. B., Boynton, W. V., Chin, G., Garvin, J. B., Golovin, D., ... Zuber, M. T. (2010, October). Hydrogen Mapping of the Lunar South Pole Using the LRO Neutron Detector Experiment LEND. *Science*, *330*(6003), 483. doi: 10.1126/science.1185696

Needham, D. H., & Kring, D. A. (2017, November). Lunar volcanism produced a transient atmosphere around the ancient Moon. *Earth and Planetary Science Letters*, *478*, 175-178. doi: 10.1016/j.epsl.2017.09.002

Noda, H., Araki, H., Goossens, S., Ishihara, Y., Matsumoto, K., Tazawa, S., ... Sasaki, S. (2008, December). Illumination conditions at the lunar polar regions by KAGUYA(SELENE) laser altimeter. *Geophysical Research Letters*, *35*, 24203. doi: 10.1029/2008GL035692

Nozette, S., Lichtenberg, C. L., Spudis, P., Bonner, R., Ort, W., Malaret, E., ... Shoemaker, E. M. (1996, November). The Clementine Bistatic Radar Experiment. *Science*, *274*, 1495-1498. doi: 10.1126/science.274.5292.1495

Ong, L., Asphaug, E. I., Korycansky, D., & Coker, R. F. (2010, June). Volatile retention from cometary impacts on the Moon. *Icarus*, *207*(2), 578-589. doi: 10.1016/j.icarus.2009.12.012

Paige, D. A., Siegler, M. A., Zhang, J. A., Hayne, P. O., Foote, E. J., Bennett, K. A., ... Lucey, P. G. (2010, Oct). Diviner Lunar Radiometer Observations of Cold Traps in the Moon's South Polar Region. *Science*, *330*(6003), 479. doi: 10.1126/science.1187726

Pieters, C. M., Goswami, J. N., Clark, R. N., Annadurai, M., Boardman, J., Buratti, B., ... Varanasi, P. (2009, October). Character and Spatial Distribution of OH/H_2O on the Surface of the Moon Seen by M^3 on Chandrayaan-1. *Science*, *326*(5952), 568. doi: 10.1126/science.1178658

Rubanenko, L., Venkatraman, J., & Paige, D. (2019, 08). Thick ice deposits in shallow simple craters on the moon and mercury. *Nature Geoscience*, *12*. doi: 10.1038/s41561-019-0405-8

Sanin, A. B., Mitrofanov, I. G., Litvak, M. L., Bakhtin, B. N., Bodnarik, J. G., Boynton, W. V., ... Vostrukhin, A. A. (2017, Feb). Hydrogen distribution in the lunar polar regions. *Icarus*, *283*, 20-30. doi: 10.1016/j.icarus.2016.06.002

Sanin, A. B., Mitrofanov, I. G., Litvak, M. L., Malakhov, A., Boynton, W. V., Chin, G., ... Zuber, M. T. (2012, June). Testing lunar permanently shadowed regions for water ice: LEND results from LRO. *Journal of Geophysical Research (Planets)*, *117*, E00H26. doi: 10.1029/2011JE003971

Schorghofer, N., & Aharonson, O. (2014, jun). THE LUNAR THERMAL ICE PUMP. *The Astrophysical Journal*, *788*(2), 169. Retrieved from `https://doi.org/10.1088%2F0004-637x%2F788%2F2%2F169` doi: 10.1088/0004-637x/788/2/169

Siegler, M., Paige, D., Williams, J.-P., & Bills, B. (2015, Jul). Evolution of lunar polar ice stability. *Icarus*, *255*, 78-87. doi: 10.1016/j.icarus.2014.09.037

Spudis, P. D., Bussey, D. B. J., Baloga, S. M., Cahill, J. T. S., Glaze, L. S., Patterson, G. W., ... Ustinov, E. A. (2013, Oct). Evidence for water ice on the moon: Results for anomalous polar craters from the LRO Mini-RF imaging radar. *Journal of Geophysical Research (Planets)*, *118*(10), 2016-2029. doi: 10.1002/jgre.20156

Thomson, B. J., Bussey, D. B. J., Cahill, J. T. S., Neish, C., Patterson, G. W., & Spudis, P. D. (2011, March). The Interior of Shackleton Crater as Revealed by Mini-RF Orbital Radar. In *Lunar and planetary science conference* (Vol. 42, p. 1626).

Thomson, B. J., Bussey, D. B. J., Neish, C. D., Cahill, J. T. S., Heggy, E., Kirk, R. L., ... Ustinov, E. A. (2012, Jul). An upper limit for ice in Shackleton crater as revealed by LRO Mini-RF orbital radar. *Geophysical Research Letters*, *39*(14), L14201. doi: 10.1029/2012GL052119

Trenberth, K. E., & Stepaniak, D. P. (2003, Nov). Seamless Poleward Atmospheric Energy Transports and Implications for the Hadley Circulation. *Journal of Climate*, *16*(22), 3706-3722. doi: 10.1175/1520-0442(2003)016⟨3706:SPAETA⟩2.0.CO;2

Vasavada, A. R., Paige, D. A., & Wood, S. E. (1999, October). Near-Surface Temperatures on Mercury and the Moon and the Stability of Polar Ice Deposits. *Icarus*, *141*(2), 179-193. doi: 10.1006/icar.1999.6175

Watson, K., Murray, B., & Brown, H. (1961, May). On the Possible Presence of Ice on the Moon. *Journal of Geophysical Research*, *66*, 1598-1600. doi: 10.1029/JZ066i005p01598

Williams, J.-P., Greenhagen, B. T., Paige, D. A., Schorghofer, N., Sefton-Nash, E., Hayne, P. O., ... Aye, K. M. (2019). Seasonal polar temperatures on the moon. *Journal of Geophysical Research: Planets*, *124*(10), 2505-2521. Retrieved from `https://agupubs.onlinelibrary.wiley.com/doi/abs/10.1029/2019JE006028` doi: 10.1029/2019JE006028

Zuber, M. T., Head, J. W., Smith, D. E., Neumann, G. A., Mazarico, E., Torrence, M. H., ... Melosh, H. J. (2012, Jun). Constraints on the volatile distribution within Shackleton crater at the lunar south pole. *Nature*, *486*(7403), 378-381. doi: 10.1038/nature11216